Pergamon

Int. J. Heat Mass Transfer. Vol. 38, No. 17, pp. 3197–3207, 1995
Copyright © 1995 Elsevier Science Ltd
Printed in Great Britain. All rights reserved
0017–9310/95 $9.50+0.00

0017–9310(95)00065–8

Heat transfer in a rectangular channel with perforated turbulence promoters using holographic interferometry measurement

JENN-JIANG HWANG†

Department of Mechanical Engineering Chung-Hua Polytechnic Institute, Hsinchu, Taiwan 30067, Republic of China

and

TONG-MIIN LIOU

Department of Power Mechanical Engineering National Tsing Hua University, Hsinchu, Taiwan 30043, Republic of China

(*Received* 4 *August* 1994 *and in final form* 26 *January* 1995)

Abstract—An experimental study is conducted to examine the effect of perforated ribs on turbulent heat transfer and friction in a rectangular channel. Perforated ribs with an open-area ratio of 50% are staggered on two opposite walls of the channel. Four rib pitch-to-height ratios (Pi/H = 5, 10, 15 and 20) and two rib height-to-channel hydraulic diameter ratios (H/De = 0.081 and 0.162) are examined. The Reynolds number ranges from 10 000 to 50 000. To facilitate comparison, results of conventional solid-type ribs are also compiled. Laser holographic interferometry is employed to measure the heat transfer coefficients of the ribbed wall. The results indicate that the perforated ribs have the advantages of eliminating the hot-spots and providing a superior heat transfer performance. Roughness friction and heat transfer correlations are also developed in terms of flow and rib parameters.

INTRODUCTION

Periodic flow interruption created in channels/pipes is a common means for heat transfer enhancement. This problem is of practical importance and widely considered in the design of devices such as heat exchangers, advanced gas-cooled reactor fuel elements and internal cooling passages of gas turbines. The flow passages of these devices are usually roughened by periodic solid-type ribs. The solid-type ribs break the laminar sublayer and create local wall turbulence due to flow separation and reattachment between the ribs, which greatly enhances heat transfer. Numerous publications have been concerned with flow in a channel with solid-type ribs mounted on one or two principal channel walls. For the sake of brevity, only the most relevant works are cited below. Burggraf [1] studied the turbulent airflow in a square duct with transverse solid-type ribs on two opposite walls for the Reynolds number ranged from 1.3×10^4 to 1.3×10^5. The effect of entrance geometry (long duct, short duct and bent entrance) on the regionally average heat transfer coefficient was examined. Webb *et al.* [2] presented heat transfer and pressure drop data for fully developed turbulent flow in circular tubes with internal transverse solid-type ribs for a wide range of Prandtl number ($0.7 \leqslant Pr \leqslant 37.6$). The geometrical parameters were varied within the ranges of $0.01 \leqslant H/De \leqslant 0.04$ and $10 \leqslant Pi/H \leqslant 40$. Based on the similarity [3], the authors successfully correlated the friction and heat transfer data for turbulent tube flow with repeated rib roughness by taking into account the geometrically non-similar roughness parameter Pi/H. The procedure involved interpreting the friction factor data in terms of Nikuradse's [3] similarity roughness function and the roughness Reynolds number, and subsequently applying the heat transfer–momentum transfer analogy to develop the general form of heat transfer coefficient. Han [4] investigated the effect of rib angle-of-attack on the average heat transfer coefficient and pressure drop in square duct flows. The results were obtained for the solid-type rib with angles-of-attack 30, 45, 60 and 90°. Ribs with angle-of-attack of 60° gave the highest heat transfer as well as the highest pressure drop, whereas 45° and 30° ribs resulted in the maximum cooling for a given pumping power. Metzger *et al.* [5] conducted an experiment to examine the effect of varying the rib angle in rib-roughened triangular ducts. Solid-type ribs were placed on two of the three walls of the test ducts to model the internal cooling passage at the leading edge of a turbine airfoil. The authors utilized thin replaceable coatings of temperature sensitive material (melt-

†Associate professor, to whom correspondence should be addressed.

NOMENCLATURE

A	half-width of channel [m]
B	half-height of channel [m]
c_p	specific heat at constant pressure [kJ kg^{-1} K^{-1}]
De	hydraulic diameter, $2B/(1+B/A)$ [m]
f	friction factor
Gd	Gladstone–Dale constant
H	rib height [m]
k_f	air conductivity [kJ m^{-1} K^{-1}]
m	mass flow rate [kg s^{-1}]
$\overline{Nu}$	local Nusselt number
$\overline{Nu}_s$	average Nusselt number for the smooth duct (at the same mass flow rate)
$\overline{Nu}_s^*$	smooth duct average Nusselt number (at the same pumping power)
$\overline{Nu}_p$	periodic fully developed (average) Nusselt number for the ribbed duct
Pi	rib pitch [m]
PR	rib pitch-to-height ratio, Pi/H
Pr	Prandtl number
q_{conv}	convective heat transfer from the wall [kJ m^{-2}]
Re	Reynolds number, UDe/v
S	fringe order
T	temperature of air [K]
T_b	local bulk mean temperature of air [K]
T_{in}	air temperature at duct inlet (i.e. room temperature) [K]
T_w	local wall temperature [K]
$\bar{T}_b$	average bulk mean temperature of air, $(\int_0^{Lh} T_b \, dX)/L_h$ [K]
$\bar{T}_w$	average wall temperature [K]
X	axial coordinate ($X = 0$ at inlet reference)
X_N	axial coordinate ($X_N = 0$ at rib rear edge)
Y	transverse coordinate
Z	spanwise coordinate.

Greek symbols

α	rib angle-of-attack
β	rib open-area ratio
λ	wavelength of the laser beam [m]
ρ	air density [kg m^{-3}]
ϕ	radius of the perforation [m].

Subscripts

b	bulk mean
i	fringe index
N	rib index
r	reference
s	smooth
w	wall.

ing point 43°C) on the test surfaces in the presence of a heated air stream to determine local surface heat transfer rates by the transient technique. It was found that the heat transfer augmentation in ribbed triangular channels was significantly higher on both the ribbed and smooth walls than in square channels. Shortening the ribs to give less flow obstruction in the corner regions did not improve heat transfer. Liou and Hwang [6] experimentally studied the effect of rib shapes on heat transfer and friction characteristics in periodic fully developed duct flows. Three rib shapes (square, triangular, and semicircular) with the same rib height ($H/De = 0.081$) were investigated in their work. The local as well as the average Nusselt numbers were determined by real-time laser holographic interferometry (LHI). It was found that the three shaped ribs had comparable thermal performances under constant pumping power constraints. Note that in the above-mentioned studies, emphases were placed on the results of the solid-type ribs.

Studies of turbulent flow and heat transfer around perforated baffles originate from Tanasawa *et al.* [7]. The resistance heating method and thermocouple technique were employed to determine the heat transfer coefficients in a channel with turbulence promoters symmetrically mounted on two opposite walls. Comprehensive comparisons were made among the three types of turbulence promoters, namely, fence-type, perforated plate-type and slitted plate-type. Results showed that surfaces with perforated plate-type turbulence promoters provided excellent performance under constant pumping power conditions. Later, Tanasawa *et al.* [8] further investigated the effect of the half-perforated turbulence promoters on the heat transfer and friction in a rectangular channel. It was found that surfaces with the half-perforated turbulence promoters with perforations on the lower half of the rib performed better than those with the solid-type and fully perforated turbulence promoters. Another important finding was that the local heat transfer coefficient decreased as a whole when fewer than two pairs of promoters elements were placed upstream. Ichimiya *et al.* [9] conducted experiments to investigate the effect of a single porous rib on the heat transfer and friction characteristics in a parallel plate duct. The porous rib was applied to the insulated wall facing the heated smooth surface. It was found that the thermal performance under constant pumping power constraints was better in the laminar region than in the turbulent region. Yamada and Osaka [10] experimentally studied the effects of plate aspect and open-area ratios on the heat transfer characteristics of the flow over a perforated plate standing on the wall. Only one flow velocity ($U = 5$ m s^{-1}) was tested in their work. An important finding made by them was that the critical open-area ratio in which there

was a circulation region behind the plate was between 0.325 and 0.485.

The purpose of the present work is to investigate the heat transfer and friction characteristics in a rectangular channel with periodic perforated ribs staggered mounted on two opposite walls. The perforated ribs with an open-area ratio 0.5 are placed transversely to the main stream direction. The heat transfer data are obtained via LHI. This technique not only is whole-field in character but also allows direct determination of the convection heat transfer to the working fluid. Thus, heat losses (containing conductive and radiative losses), which usually exist in heat transfer experiments, can be characterized, quantified and corrected. Moreover, it is a useful flow-visualization technique to characterize the flow structure in ducts with complex rib geometries. Four objectives are carried out in this work. First, experiments are carried out to determine the local heat transfer distributions in the periodic flows, which enables the assessment of the possibility of hot-spots on the ribbed wall. It is well-known that a separation bubble attached to the rib rear will create a region where wall heat transfer deteriorates [6]. Thus, it is important to investigate whether an improved heat transfer in the recirculating region can be obtained when perforated ribs are applied on the heated wall. Then, the effect of replacing solid-type ribs by perforated ribs on the average heat transfer and friction in a channel is investigated. Third, by employing the average heat transfer and friction data, a performance analysis based on identical pumping power constraint is made. Finally, roughness correlations for heat transfer and friction are developed. These correlations may be helpful for the design of related devices such as heat exchangers, gas turbine airfoils, and electronic cooling packages.

EXPERIMENTAL FACILITY

Flow circuit

The experiments are performed in an open-loop airflow system, which is shown schematically in Fig. 1. The airflow is sucked from the temperature controlled room into the test section through a settling chamber and a nozzle-like contraction. These arrangements can provide a fairly uniform flow with turbulence intensity less than 1% in the test section inlet. The uniformity of the flow and turbulence level were checked by LDA measurements. After traversing the test section, air flows through a flow straightener and a flowmeter, and is then exhausted by a 3 hp blower.

Laser holographic interferometer

The laser holographic interferometer employed in the present work is a real-time mode (single-exposure method) and is illustrated in Fig. 2. The laser used is a high-power, argon-ion laser (1), Spectra-Physic Model 2000. After passing through a shutter, the laser beam is divided into two equal components by a variable-silvered mirror (i.e. a beam splitter, 3). One beam, the reference beam, bypasses the test section and is expanded and filtered by a spatial filter (5). The expanded wave is subsequently collimated to a planar wave by a collimating lens (6). The other beam, the object beam, is also expanded, filtered and collimated to a planar wave by a spatial filter and a collimating lens. Both the planar waves fall onto the holographic plate (7) with an angle of 30°. Before the ribbed walls are heated, the hologram is exposed thereby recording the comparison wave. When the planar object wave passes through the heated test section, it is distorted as a result of the refractive index field generated by local temperature variation in the test section. The distorted object wave passes through the hologram, and there is continuous interference behind it from the comparison beam reconstructed by the reference wave. Thus an instantaneous interference field forms behind the hologram plate. A combination of the holographic film plate holder and a liquid gate is used to provide in-place development of the film plate as required for subsequent real-time work. The photographic emulsion 8E56 made by Agfa-Gevaert Ltd is found to be a suitable recording material for combining a good compromise between light sensitivity and resolution. To adjust the unwanted interference fringes caused by a shrinkage of the photographic emulsion in the developing and fixing processes, the liquid gate associated with the film plate holder is mounted on a multi-axes micropositioning base. This arrangement is designed to provide striation-free submicron positioning of the hologram in linear (three orthogonal axes) and rotational directions. The instantaneous interference field is digitized by a CCD camera (COHU, Model 6400), which allows 512×512 pixel resolution with 256 grey levels per pixel, and is recorded on a VHS videocassette recorder for storage and further image processing.

Test section

Figure 1 shows the coordinate system, structure, and dimension of the test duct. The test duct is 1200 mm long and has a rectangular cross section of 40 mm by 160 mm (YZ plane). The perforated ribs are attached in a staggered fashion to the top and bottom walls (aluminum plates, 3 mm in thickness) of the test ducts. The rib angle-of-attack is 90°. Aluminum plates and ribs are adopted in this work for their high conductivity and machinability. Thermofoils of thickness 0.18 mm are adhered uniformly between the aluminum plate and a 6 mm thick fiberglass board to ensure good contact. In addition, two pieces of balsa wood (20 mm thick) are used to prevent heat loss from the upper and lower sides of the heated plates. A thin layer of glue (0.13 mm thick or less) serves at each of the above-mentioned interface to ensure good contact. The thermal resistance of the glue may be neglected (less than 1%). The region of optical view is instrumented with 28 copper–constantan thermocouples distributed along the spanwise centerline ($Z = 0$) of the heated plate and ribs for wall temperature

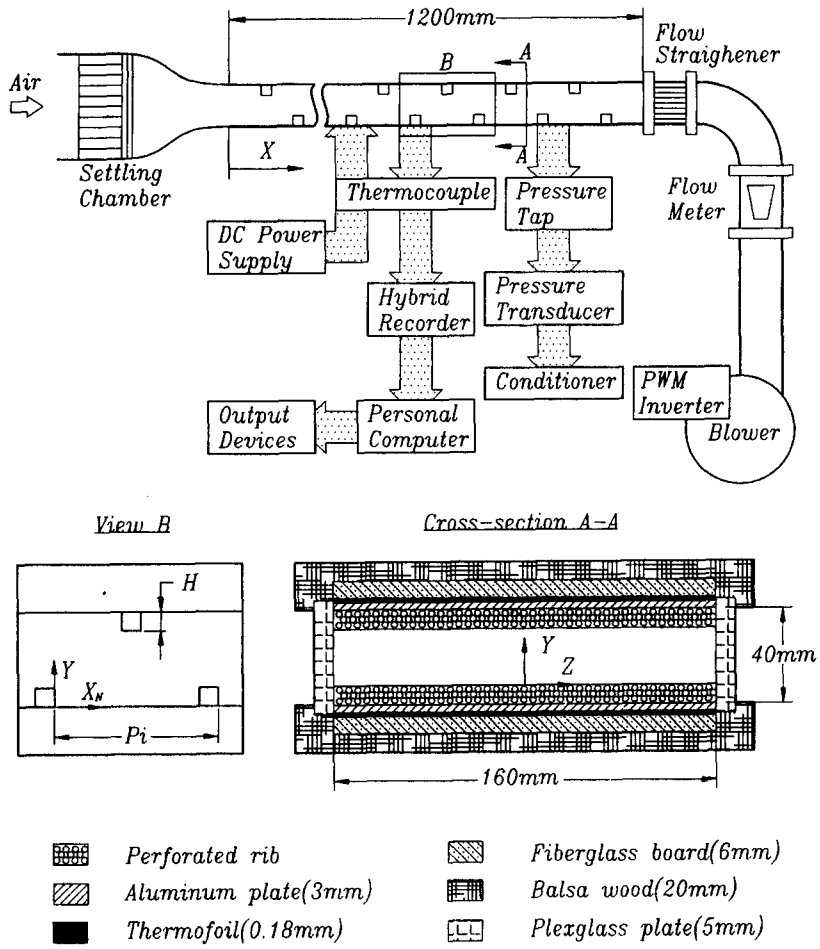

Fig. 1. Schematic drawing of the experimental apparatus, structure and coordinate system of the test section.

measurements, as shown in Fig. 3. The junction-beads (0.15 mm in diameter) are carefully embedded into the wall, and then ground flat to ensure that they are flush with the surfaces. The temperature signals are transferred to a hybrid recorder (Yokogawa, DA-2500), and all data are then sent to a PC-AT via GBIB interface. The pre-processing of the raw data can be carried out using a built-in BASIC program by which

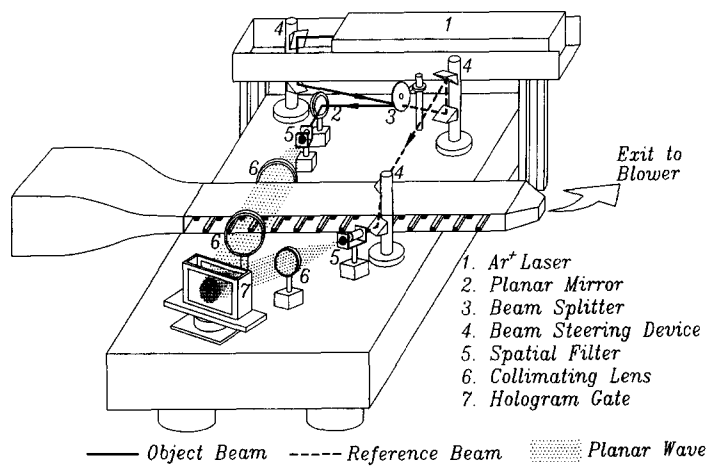

Fig. 2. Schematic drawing of the laser holographic interferometer.

Fig. 3. Photographs of the investigated perforated and solid-type ribs.

the non-dimensional parameter can be calculated. In addition, two pressure taps are used to measure the static pressure for the fully developed duct flows. Each tap is connected with a microdifferential transducer (Kyowa, PDL-40B). The measured pressure signal is subsequently read from the conditioner (Kyowa, WGA-200A).

Figure 3 shows a photograph of the perforated and solid-type ribs investigated in the present work. The open-area ratio of the perforated rib, which is defined as $\beta = n\pi\phi^2/(2AH)$, is 50%. The rib thickness is fixed at 4 mm. The other interesting parameters include: the rib pitch-to-height ratio, $PR = 5$, 10, 15, and 20; the Reynolds number (based on the duct hydraulic diameter and bulk mean velocity), $1.0 \times 10^4 \leqslant Re \leqslant 5.0 \times 10^4$; and the rib-to-channel height ratio (or the ratio of the rib height-to-channel hydraulic diameter) $H/2B = 0.13$, and $0.26(H/De = 0.081$, and 0.162).

EXPERIMENTAL CONDITIONS AND DATA ANALYSIS

Fully developed conditions

Since periodic fully developed heat transfer and friction characteristics in a ribbed channel are interesting in the present study, the interferometry and pressure drop data are taken between $X/De = 12$–14.2 and 6–18 respectively. The hydrodynamic and thermal periodicity in this region has been verified elsewhere [11], and thus is not elaborated on in this work.

Two-dimensionality

In applying LHI, it is necessary to ensure that the temperature distributions along the test section width (Z direction) in the flow field are two dimensional because the holographic interferometry technique is based on the integral of the change in spanwise refractive index. The significant errors usually encountered in the interferometric experiments are not only due to the end effect, but also to the refraction effect. The former is caused by deviation from two-dimensionality of the actual temperature field, whereas the latter occurs when there is a density gradient normal to the light beam causing the beam to bend, and the resulting error increases with increasing disturbed length (Z direction). Thus, if an experimental apparatus is designed to minimize the end-effect error (increasing the optical path length), the refraction-effect error may be large, and *vice versa*. The aspect ratio of the channel used in this work is 4:1 for a reasonable combination of the end-effect and refraction-effect errors. By using the interferometry error analysis suggested in Goldstein [12], it is found that the resulting errors in the fringe (or temperature) shift due to the end effect and the refraction effect are about 8% and 4.2%, respectively. The same aspect ratio is employed in Walklate [13] for the study of two-dimensional thermal boundary layers and in Lockett and Collins [14] for the study of rib-roughness channel flows. Nevertheless, the two-dimensionality of the spanwise temperature profile of the flow field is checked by thermocouple probing in this study. The scatter in the spanwise direction was less than 6% of the channel spanwise average temperature.

Fringe analysis

To determine the temperature field described by the interferogram, the equation of interferometry for a two-dimensional incompressible flow is as follows [15]:

$$S_i - S_{i-1} = T_r \rho_r Gd 2A(1/T_{S_i} - 1/T_{S_{i-1}})/\lambda \qquad (1)$$

where $S_i - S_{i-1}$ is the fringe shift, S_i the fringe order, Gd the Gladstone–Dale constant, and ρ_r the air density evaluated at reference temperature T_r. By setting $S_i - S_{i-1} = 1$, the temperature differences $T_i - T_{i-1}$ associated with each fringe are determined. Knowledge of at least one temperature and the temperature difference in the region of interest will provide the approximate heat transfer feature from wall to air.

Heat transfer coefficient

In this study, the entire temperature field is revealed by infinite-fringe interferometry, which then enables calculation of the local heat transfer coefficients of the heated surface. The convection heat transfer coefficient can be presented in terms of the local Nusselt number Nu, which is defined as

$$Nu = -(\mathrm{d}T/\mathrm{d}Y)_w De/(T_w - T_b) \qquad (2)$$

where $(\mathrm{d}T/\mathrm{d}Y)_w$ is determined by curve fitting, based on a least-squares method through the near-wall values for temperature and fringe shift; T_w is read from the thermocouple output; and T_b is calculated from an energy balance, $T_b = T_{in} + Q/(mc_p)$, where Q

is the quantity of heat given to air from the entrance to the considered cross section of the duct and can be obtained by the integrated form of

$$\int_0^x [k_f(\mathrm{d}T/\mathrm{d}Y)_w 2A]\,\mathrm{d}X.$$

The maximum uncertainty of the local Nusselt number is estimated to be less than 6.5% by the uncertainty estimation method of Kline and McClintock [16].

The average Nusselt number is evaluated by the following equation

$$\overline{Nu}_p = q_{conv} De/[k_f(T_w - T_b)] \quad (3)$$

where q_{conv} is estimated by subtracting the heat loss from the supplied electrical input. The maximum uncertainty of $\overline{Nu}_p$ was estimated to be less than 9.8%. The local and average Nusselt numbers of the present study are normalized by the Nusselt number for fully developed turbulent flow in smooth circular tubes correlated by Dittus and Boelter [17]:

$$\overline{Nu}_p/\overline{Nu}_s = \overline{Nu}_p/(0.023 Re^{0.8} Pr^{0.4}). \quad (4)$$

The friction factor of the periodic fully developed flow is expressed as:

$$f = [(-\Delta P/\Delta X)\cdot De/4]/(\rho U^2/2) \quad (5)$$

where the pressure gradient, $\Delta P/\Delta X$, is evaluated by taking the ratio of the pressure difference and the distance of two successive pressure taps. The maximum uncertainty of f is estimated to be less than 7.3%.

Roughness functions

The friction data for turbulent flow in a rectangular duct with two opposite ribbed walls can be correlated by the modified equations [4, 6]:

$$R(H^+) = (f/8)^{-1/2} + 2.5 \ln\{(2H/De) \times [2A/(A+B)]\} + 2.5 \quad (6)$$

where

$$H^+ = (H/De) Re (f/8)^{1/2}. \quad (7)$$

The heat transfer data for fully developed turbulent flow in a rectangular duct with two opposite ribbed walls can be correlated by the following equation:

$$G(H^+, Pr) = (f/8)^{1/2}/St + 2.5 \ln\{(2H/De)/[2A/(A+B)]\} + 2.5. \quad (8)$$

In the present data reduction program, equations (6)–(8) are used to calculate the friction roughness function $R(H^+)$ and the heat transfer roughness $G(H^+, Pr)$.

RESULTS AND DISCUSSION

Interference patterns

Two categories of the interferometric results are presented in the present work, namely, finite-fringe and infinite-fringe interferences. Typical examples of the finite- and infinite-fringe interferograms are shown in Figs. 4(a)–(c) and (d)–(e) respectively. Figure 4(a) is a reference interferogram without any disturbance in the field, where parallel, equally spaced and alternately dark and bright fringes appear. When disturbances are present with the test section, the optical path is no longer uniform. The fringes then are no longer straight, but curved. A comparison of the disturbed finite-fringe interferogram around the perforated rib and that around the solid-type rib is shown in Figs. 4(b) and (c). For the solid-type rib, there is no fluid passing through the rib, and the total flow has to turn from the duct wall into the contraction between the rib and the opposite wall. Therefore, a strong shear layer initiated from the rib upstream corner is introduced by the main flow, which drives the recirculating flow behind the rib. This can be observed from the highly distorted fringes in the regions of the flow over and behind the rib top. Note should be taken in this figure that the fringes near the duct wall behind the rib are distorted insignificantly, and are roughly perpendicular to the duct walls. This signifies that the heat transfer rate on the duct wall is very small. As for the perforated rib, saw-shaped fringes are found behind the rib. They reveal that a part of fluid penetrates the rib, and the recirculating cell behind the rib disappears. In addition, the distortion of the fringes near the duct wall behind the perforated rib is more noticeable than that behind the solid-type rib. The transport phenomenon in this region is indeed improved when the solid-type ribs are replaced by the perforated ribs on the duct wall. Additional outcomes will be shown later for the comparison of local Nusselt number distributions. Figures 4(d) and (e) are typical isotherm-pattern interferograms (infinite-fringe set) for the solid-type and perforated rib geometries respectively. From the information of the whole-field air temperature distributions given by the interferograms (infinite-fringe set), the local heat transfer coefficient of the ribbed walls can be calculated.

Local Nusselt number

A comparison of the distributions of the local Nusselt number ratio along the perforated and solid-type ribbed walls is shown in Fig. 5. The Reynolds number, rib height-to-channel hydraulic diameter ratio, and rib pitch-to-height ratio are kept at values of 40 000, 0.081 and 10, respectively. As for the results between the ribs, it can be seen that the difference of the $Nu/\overline{Nu}_s$ distributions along the perforated and solid-type ribbed walls is evident. The results of the duct with solid-type ribs have been described in detail by Liou and Hwang [6] and are not elaborated on in the present paper. For the distribution on the perforated ribbed wall, it starts with a local maximum, is followed by a decrease, then reaches another local maximum before a final gradual decrease. The first local maximum is believed to be caused by the effect of the intense jet-turbulence generated from the rib rear.

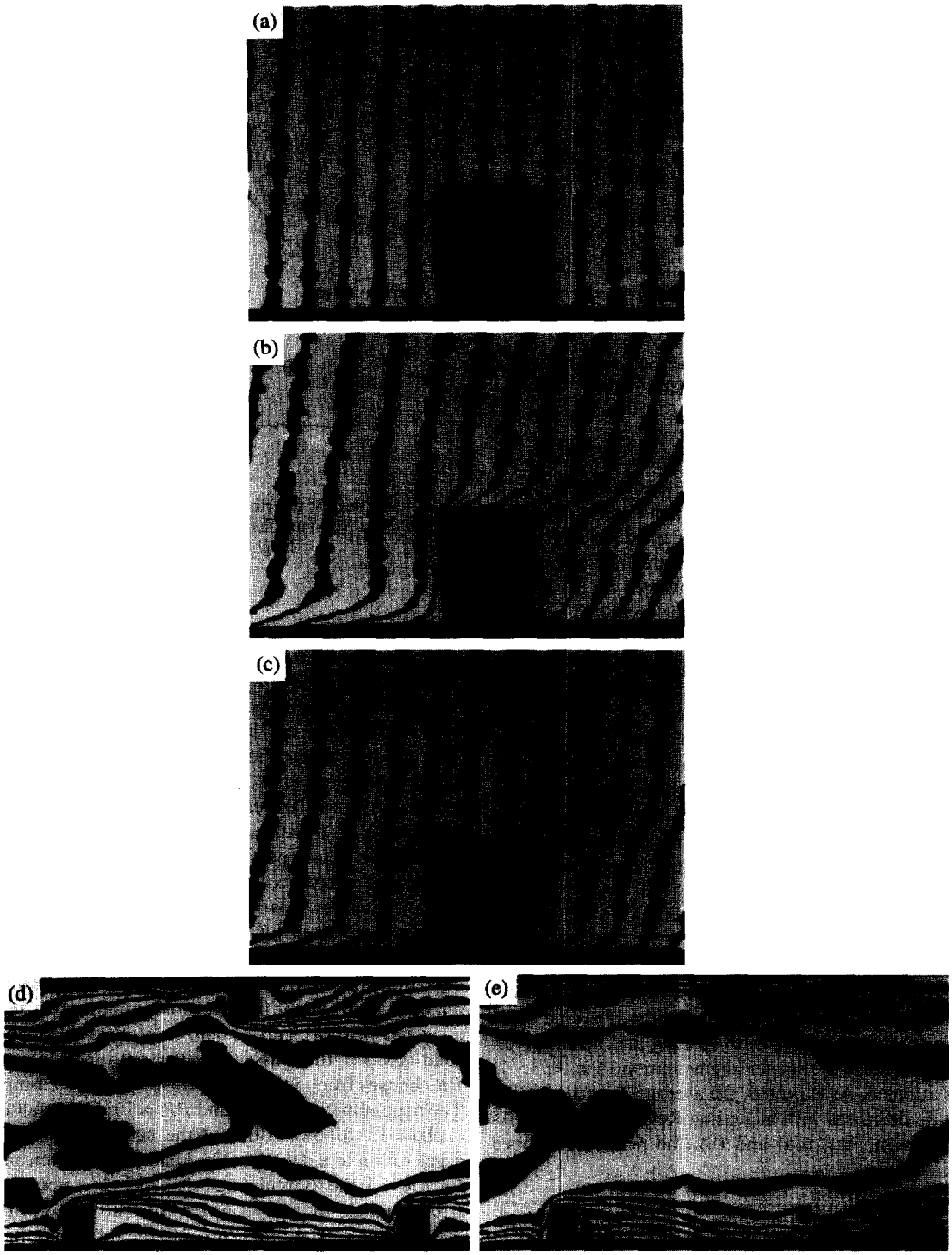

Fig. 4. Examples of the holographic interferograms. (a) Undisturbed finite fringe pattern. (b) $Re = 2.0 \times 10^4$, $PR = 10$, $H/De = 0.081$, solid-type rib (finite fringe). (c) $Re = 2.0 \times 10^4$, $PR = 10$, $H/De = 0.081$, perforated rib (finite fringe). (d) $Re = 2.0 \times 10^4$, $PR = 10$, $H/De = 0.081$, solid-type rib (infinite fringe). (e) $Re = 2.0 \times 10^4$, $PR = 10$, $H/De = 0.081$, perforated rib (infinite fringe).

This can be assessed by qualitative observation of the highly fluctuating fringes in this region. The second maximum located in the middle of the successive ribs is considered to be a result of flow acceleration caused by the sudden contraction of the flow passage. On the rib top, similar trends of the $Nu/\overline{Nu}_s$ distribution are obtained for the perforated and solid-type ribbed geometries. There exits a local maximum of $Nu/\overline{Nu}_s$ on the upstream rib corner due to forced convection augmented by flow acceleration and there follows a rapid

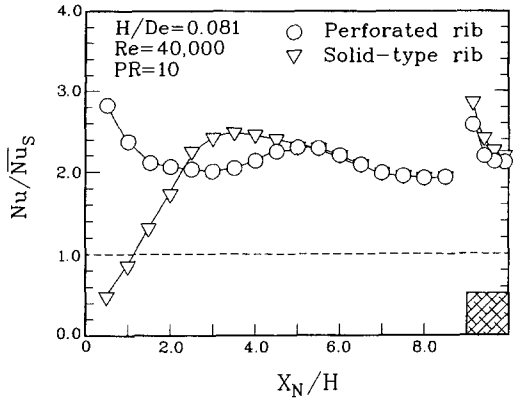

Fig. 5. Comparison of local Nusselt number distributions along the perforated and solid-type ribbed surfaces.

decrease because of the development of the thermal boundary layer. Note that the level of $Nu/\overline{Nu}_s$ for the perforated rib is slightly lower than that for the solid-type rib. The reason may be explained as follows: for the perforated rib a large amount of heat conducted from the rib base has been convected by the airflow through the rib, and therefore the conductive heat to the rib top (or convective heat from the rib-top surface to the test section) is reduced. These results can be confirmed by comparing the fringes near the top wall of the solid-type and perforated ribs. As shown in Figs. 4(b) and (c), the distortion degree of fringes near the top wall of the solid-type rib is more significant than those near the perforated-rib top. An important finding observed in Fig 4 is that the hot-spots ($Nu/\overline{Nu}_s < 1$) around the concave corner behind the solid-type rib do not appear in the corresponding region for the perforated-ribbed wall.

Average Nusselt number

Figure 6 gives the average Nusselt number ratio of the perforated and solid-type ribbed walls as a function of Reynolds number. It can be observed from this figure that for the rib spacing and height investigated the heat transfer augmentation ($\overline{Nu}_p/\overline{Nu}_s > 1$) is attained. As expected, the average Nusselt number ratio decreases with increasing Reynolds number. As shown in Figs. 6(a) and (b), the perforated ribbed

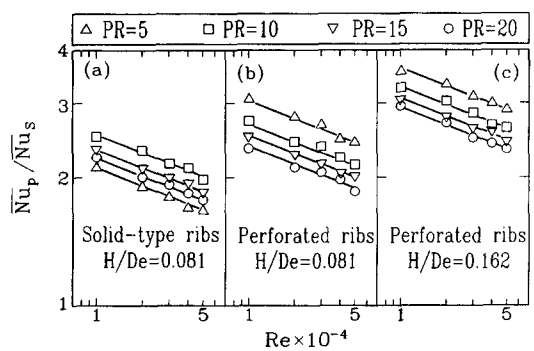

Fig. 6. Average Nusselt number ratio vs Reynolds number.

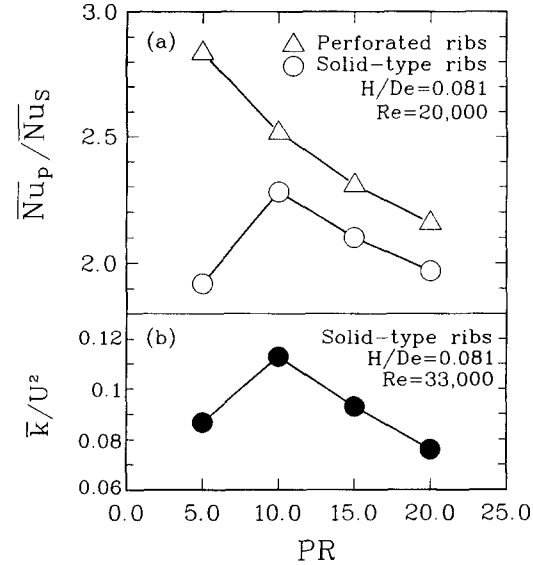

Fig. 7. (a) Effect of the rib spacing on the average Nusselt number ratio. (b) Turbulent kinetic energy vs rib pitch-to-height ratio [18]

geometry provides a higher Nusselt number ratio than the solid-type rib with the same rib height ($H/De = 0.081$) over the range of the Reynolds number studied, typically about 10–40% for $PR > 10$ and 60–80% for $PR = 5$. The comparison between Figs. 6(b) and (c) further shows that the average Nusselt number ratio increases with rib height for the perforated rib. A similar trend was obtained for the solid-type rib [6]. As for the effect of rib spacing, the tendency for the solid-type rib is quite different from that for the perforated rib, as will be described below.

Typical results showing the effect of rib spacing on the average Nusselt number ratio for the perforated and solid-type ribbed geometries are plotted in Fig. 7(a). In this figure the rib height-to-channel hydraulic diameter ratio and the flow Reynolds number are fixed at values of 0.081 and 20 000, respectively. For the solid-type rib, the Nusselt number ratio increases as PR changes from 5 to 10, and then starts decreasing. The maximum value is around $PR = 10$. The result is explained as follows. Although the increase of the flow acceleration in a densely ribbed channel is significant for $PR = 5$, the recirculating cell, which does not contribute much to heat transfer, fills up the cavity between the ribs. As for $PR = 10$, the flow separates from the rib upstream from it, and then reattaches to the duct wall. Generally, the reattached flow causes higher heat transfer, by enhancing turbulence, than does the cavity flow. This can be supported by the close correlation of the heat transfer coefficient and turbulent kinetic energy distributions [18], as shown in Figs. 7(a) and (b). Therefore, the distribution of the average Nusselt number for the solid-type rib is reasonable. In contrast to the results of the solid-type ribbed geometry, the average Nusselt number ratio for the perforated ribbed geometry decreases mon-

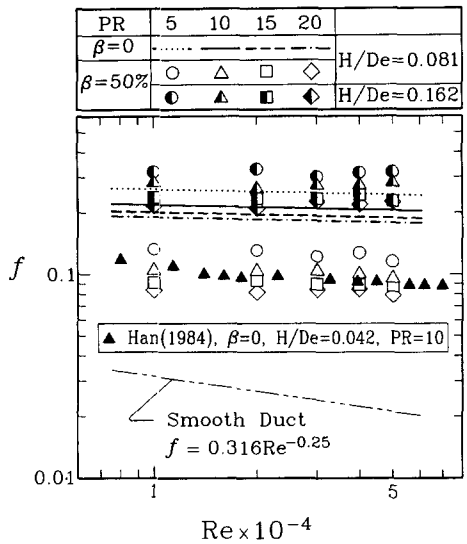

Fig. 8. Friction factor vs Reynolds number.

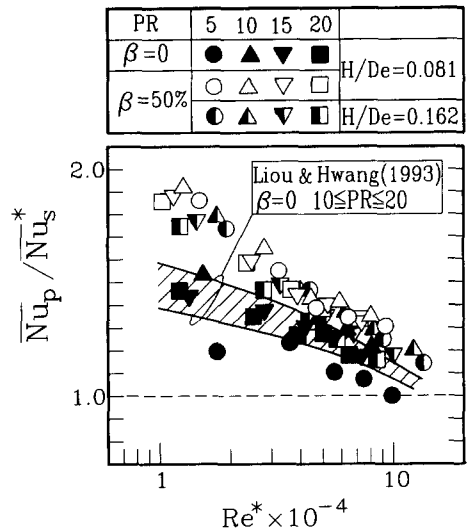

Fig. 9. Performance of the ribbed ducts at the same pumping power constraint.

otonously with the increase of PR from 5 to 20. This is because the flow patterns around the perforated ribs are similar throughout the PR range investigated. That is, airflow partly penetrates through the perforated ribs to produce multi-round-jets on the rib rear [19]. Thus, the heat transfer enhancement is affected only by the frequency of flow disturbance, which decreases with increasing PR.

Friction factor

The Reynolds number dependence of friction factor for various rib spacings and heights is displayed in Fig. 8. In this plot the friction factor correlation for the fully developed flow in a smooth circular tube (Blasius correlation) is also displayed for comparison. To avoid the figure being over-crowded, the results of the solid-type rib with $H/De = 0.081$ are presented as various types of lines, which are correlated from experiment. As shown in Fig. 8, the friction factor stays almost at a constant value when the Reynolds number varies. The perforated rib has a much smaller friction factor than the solid-type ribbed geometry when the rib height and spacing are fixed. This is reasonable because of the smaller cross-sectional blockage for the perforated ribs. As compared with the smooth duct results, the friction factor for $H/De = 0.081$ is about 4–6 and 6–9 times that for the perforated and solid-type ribbed ducts, respectively. As for the effect of rib height, the friction factor increases with increasing H/De for a given PR and Re. It is interesting to make a comparison between the friction factor in the perforated and solid-type ribbed channels with the same cross-sectional blockage but different rib height. As shown in Fig. 8, the perforated ribbed channel with $H/De = 0.162$ (half-open symbols) has the same channel blockage as the solid-type ribbed channel with $H/De = 0.081$ (various types of lines). However, the friction factor for the perforated ribbed channel is slightly higher than that of the solid-type channel. This may be due to a higher surface drag accompanying the perforated ribbed channel, which is caused by the flow through the perforations. A comparison of the present data with those in previous work [20] is also made in Fig. 8. In Han's work, solid-type ribs with $H/De = 0.042$ and $PR = 10$ are arranged on the two opposite channel walls symmetrically. The channel blockage nearly equals that of $H/De = 0.081$ and $\beta = 50\%$ in the present work. It can be shown that there is satisfactory agreement between these two works.

Performance comparison

A general tendency found in the previous discussion of the solid-type rib is that the value of f is large when $\overline{Nu}_p$ is large. From the results of the slightly higher heat transfer augmentation and evidently lower pressure drop penalty for the perforated ribbed geometry, superior thermal performance at constant pumping power condition may be expected. To maintain the fluid through the duct, the pumping power required is mP/ρ, which can be further reduced to fRe^3. Thus in Fig. 9 the performance is plotted against $[f/(0.316Re^{-0.25})]^{1/3}Re$ (denoted as Re^*). It is obvious that at lower Reynolds number both the perforated and solid-type ribbed geometries yield higher thermal performance than those at higher Reynolds number. As for the solid-type rib (solid symbols), the present results for $10 < PR < 20$ are compared with those of the previous work [6], and a reasonable agreement is achieved. In the case of $PR = 5$, the values of $\overline{Nu}_p/\overline{Nu}_s^*$ are significantly lower than those of $PR > 10$ because of the lower heat transfer augmentation and higher friction penalty followed by $PR = 5$. Figure 9 further shows that the improvement in the Nusselt number ratio of the perforated ribbed duct is more pronounced than that of the solid-type ribbed duct.

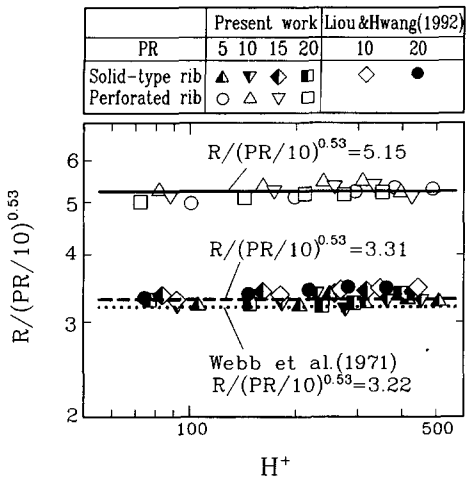

Fig. 10. Roughness friction function vs roughness Reynolds number.

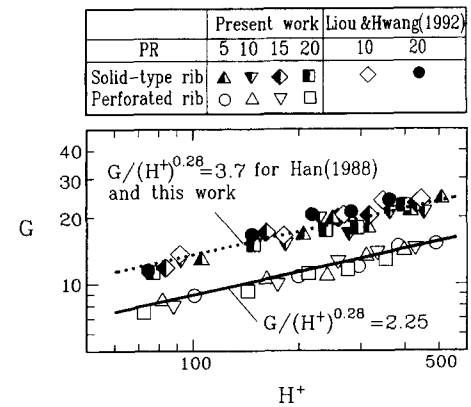

Fig. 11. Roughness heat transfer function vs roughness Reynolds number.

Roughness friction and heat transfer functions

For the results of the rectangular channel with perforated turbulence promoters to be most useful for designers, general correlations are required for both the heat transfer and friction over a wide range of rib and flow parameters. According to the friction similarity law derived in equation (6), the measured average friction factor, the rib height-to-channel hydraulic diameter ratio and Reynolds number could be correlated with the friction roughness function $R(H^+)$. A plot of $R(PR)^{0.53}$ vs roughness Reynolds number H^+ is shown in Fig. 10. The published friction data by Liou and Hwang [6] for fully developed turbulent flow in a rectangular duct with two symmetric opposite ribbed walls are also correlated using equation (6) and included in Fig. 10. The correlation of the friction roughness function R can be written as

$$R = 3.31(PR/10)^{0.53} \quad \text{for the solid-type rib} \tag{9}$$

$$R = 5.15(PR/10)^{0.53} \quad \text{for the perforated rib.} \tag{10}$$

The deviations of equations (9) and (10) are 5 and 6% respectively for 95% of the data shown in Fig. 10. Note that R in the above equations is independent of H^+. This implies that for both the perforated and solid-type ribbed geometries the average friction factor is almost independent of Reynolds number. Figure 10 further shows that the perforated ribbed geometry has higher values of R than the solid-type ribbed geometry, which shows that the perforated ribbed geometry has lower friction losses than the solid-type geometry. A comparison of the present solid-type ribbed results with the previous correlation by Webb *et al.* [2] for tube flows with solid-type ribs is also made in Fig. 11. It can be seen that the two correlations can be deemed to be identical, with a slight change of the constant. After R is correlated experimentally from equations (9) and (10), the average friction factor for the solid-type and perforated ribbed duct can be predicted by equations (6), (9), and (10) for a given rib spacing, height and channel aspect ratio.

Similarly, according to the heat transfer similarity law derived in equation (8), the measured average Nusselt number $\overline{Nu}_p$, the average friction factor f and R could be correlated with the heat transfer roughness function $G(H^+, Pr)$. A plot of G vs H^+ is shown in Fig. 11. Again, the published heat transfer data by Liou and Hwang [11] are correlated by using equation (8) and included in Fig. 11. For a Prandtl number of 0.703 in the present study, the data may be correlated as the following equations

$$G = 3.72(H^+)^{0.35}(PR/10)^{0.08} \quad \text{for the solid-type rib} \tag{11}$$

$$G = 2.25(H^+)^{0.35}(PR/10)^{0.08} \quad \text{for the perforated rib.} \tag{12}$$

The deviations of equations (11) and (12) are respectively 7 and 8% for 95% of the data shown in Fig. 11. For both the solid-type and perforated ribbed geometries, G is highly dependent on H^+ and nearly independent on PR (may be negligible). Figure 11 further shows that the values of G for the perforated ribbed geometry are lower than those for the solid-type geometry. This implies that the perforated ribbed geometry has a higher heat transfer coefficient than the solid-type ribbed geometry. As shown in Fig. 11, the correlation for the present solid-type ribbed results is identical to Han's correlation [4]. After the heat transfer roughness functions for the solid-type and perforated ribbed geometries are correlated experimentally from equations (11) and (12), respectively, the average heat transfer coefficients for the solid-type and perforated ribbed geometries can be predicted by equations (7), (8), (11) and (12) for a given rib height, Reynolds number and channel aspect ratio.

SUMMARY AND CONCLUSIONS

Local and average heat transfer characteristics in a rectangular channel with perforated ribs mounted in

a staggered fashion on two opposite walls have been performed using LHI. Since a part of the airflow passes through the perforated rib and directly impinges on the recirculating bubble behind the rib, hot-spots occurring in the region around the concave corner behind the solid-type rib do not arise in the corresponding region of the perforated-rib geometry. As compared with the conventional solid-type rib results, the average Nusselt number and friction factor of the perforated rib geometry are, respectively, about 115 and 60% in the range $10\,000 \leqslant Re \leqslant 50\,000$ with similar rib height and spacing. The slightly higher heat transfer coefficient and significantly lower pressure drop accompanying the perforated rib reflect a higher thermal performance. The friction and heat transfer roughness correlations for the perforated ribbed geometry are developed for the first time. These correlations are valid for $H^+ > 50$ and $5 \leqslant PR \leqslant 20$ and may be helpful for the design of related devices such as compact heat exchangers and turbine airfoil cooling passages.

Acknowledgement—Support for this work was provided by the National Science Council of the Republic of China under contract no. NSC 82-E0113-E-216-31-T.

REFERENCES

1. F. Burggraf, Experimental heat transfer and pressure drop with two-dimensional discrete turbulence promoters applied to two opposite walls of a square tube. In *Augmentation of Convective Heat and Mass Transfer* (Edited by E. E. Bergles and R. L. Webb), pp. 70–79. ASME, New York (1970).
2. R. L. Webb, E. R. G. Eckert and R. J. Goldstein, Heat transfer and friction in tubes with repeated-rib roughness, *Int. J. Heat Mass Transfer* **14,** 601–617 (1971).
3. J. Nikuradse, Laws for flow in rough pipes, NACA TM (1929).
4. J. C. Han, Heat transfer and friction characteristics in rectangular channels with rib turbulators, *Trans. ASME, J. Heat Transfer* **110,** 321–328 (1988).
5. D. E. Metzger, R. P. Vendula and D. D. Breen, Effects of rib angle and length on convection heat transfer in rib-roughened triangular duct. *Proc. the ASME/JSME Thermal Joint Conference*, Honolulu, HI, Vol. 3, pp. 327–333. ASME, New York (1987).
6. T. M. Liou and J. J. Hwang, Effects of ridge shapes on turbulent heat transfer and friction in a rectangular channel, *Int. J. Heat Mass Transfer* **36,** 931–940 (1993).
7. T. Tanasawa, S. Nishio, K. Takano and M. Tado, Enhancement of forced convection heat transfer in a rectangular channel using turbulence promoters, *Proc. ASME/JSME Thermal Engineering Joint Conference*, pp. 395–402 (1983).
8. T. Tanasawa, S. Nishio, K. Takano and H. Miyazaki, High-performance surface for forced-convection heat transfer using novel turbulence promoters, *ASME Paper*, 84-HT-69 (1984).
9. K. Ichimiya, M. Katayama, T. Miyazawa and H. Kondoh, Experimental study on effects of a single porous-type roughness element in a parallel plate duct, *Experimental Heat Transfer* **4,** 319–330 (1992).
10. H. Yamada and H. Osaka, Flow around a permeable rectangular plate standing vertically on the flat wall, 2nd report, effects of the aspect and the open area ratios, *Trans. JSME* **56,** 120–128 (1992).
11. T. M. Liou and J. J. Hwang, Developing heat transfer and friction in rectangular ribbed duct with flow separation at inlet, *Trans. ASME, J. Heat Transfer* **114,** 565–573 (1992).
12. R. J. Goldstein, Optical measurement of temperature. In *Measurements in Heat Transfer* (Edited by E. R. G. Eckert and R. J. Goldstein), 2nd Edn, pp. 241–294. Hemisphere, Washington, DC (1976).
13. P. J. Walklate, A two wavelength holographic technique for the study of two-dimensional thermal boundary layers, *Int. J. Heat Mass Transfer* **24,** 1051–1057 (1981).
14. J. F. Lockett and M. W. Collins, Holographic interferometry applied to rib-roughness heat transfer flow, *Int. J. Heat Mass Transfer* **33,** 2439–2449 (1990).
15. W. Hauf and U. Grigull, Optical method in heat transfer, *Advances in Heat Transfer* (Edited by J. P. Hartnett and Jr. T. F. Irvine), Vol. 6, pp. 133–136. Academic, New York (1970).
16. S. J. Kline and F. A. McClintock, Describing uncertainties on single-sample experiments, *Mech. Engng* **57,** 3–8 (1953).
17. F. W. Dittus and L. M. K. Boelter, *Publications in Engineering*, Vol. 2, p. 443, University of California at Berkley (1930).
18. T. M. Liou, J. J. Hwang and S. H. Chen, Simulation and measurement of enhanced turbulent heat transfer in a channel with periodic rib on one principal wall, *Int. J. Heat Mass Transfer* **36,** 507–517 (1993).
19. J. J. Hwang and T. M. Liou, Effect of permeable ribs on turbulent heat transfer and friction in a rectangular channel, *Trans. ASME, J. Turbomachinery* **117,** 265–271 (1995).
20. J. C. Han, Heat transfer and friction in channels with two opposite rib-roughened walls, *Trans. ASME J. Heat Transfer* **106,** 774–781 (1984).